



A multiresolution approach to enhance small telescope data under non-ideal conditions

S. CHAKRABORTY^{1,*}, T. MONDAL¹, A. DEBNATH² and S. ROYCHOWDHURY²

¹Department of Physics, Indian Institute of Technology Kharagpur, Kharagpur, India.

²Department of Physics, St. Xavier's College (Autonomous), Kolkata, India.

Corresponding author. E-mail: sabyasachi.sch@gmail.com

MS received 9 January 2021; accepted 27 December 2021

Abstract. Astronomical imaging of a star cluster is one of the paramount ways to learn about stellar evolution, stellar dynamics. A large telescope is not generally accessible to all observers. In that context, small telescope observations with a proper denoising scheme can be an excellent alternative. This paper proposes a technique to denoise star cluster data using an undecimated wavelet transform, with a modified thresholding process. Our work aims to prove the effectiveness of such a wavelet-based technique on real-time data. We present drastically noise-infested observational data of the NGC 2301 star cluster, captured over five nights from Fr. Eugene Lafont Observatory, Kolkata. We observe that for highly noise-polluted data, the conventional methods of dark frame subtraction and flat frame division are inadequate to produce the desired quality of images due to functioning exclusively in the spatial domain. Thus, we take the wavelet-based multiresolution approach to ameliorate those raw images. We also introduce a modified thresholding function to modulate the image at different resolution levels. A standard star detecting software Daophot II quantifies the increment in the number of detected stars from raw images to the images processed by our proposed method as: for red filter 397–903, for green filter 663–945, for blue filter 362–896. On the contrary, Daophot II can't detect any star in the highly noise-polluted images processed by the conventional methods. Therefore, we hope our proposed processing methodology will motivate others to initiate small telescope observations from any site restrained by its geographical location.

Keywords. Observational—data analysis—astronomy—photometric—real-time data—wavelet transform—multiresolution signal processing—Hertzsprung–Russell diagram.

1. Introduction

Astronomical imaging is one of the most important methods to learn about stellar evolution as a whole (Miles 1998). Star clusters provide magnificent pathways to explore several principles of stellar evolution and exhibit immense importance to investigate models of stellar dynamics (Vesperini 2010). Astronomical images are considerably different from typical images. They contain few components, such as a fewer number of stars in a night sky. So the imaging techniques also differ in many remarkable aspects from those used in other fields (Saha 2002).

Observing very distant and faint astronomical objects require ideal observational sites along with sensitive observational instruments. As for images of astronomical objects, various forms of noise corrupt the data. The observational work presented in this paper has been executed from an observational site located amidst the metropolitan city Kolkata (Fr. Eugene Lafont Observatory, St. Xavier's College (Autonomous), Kolkata; 22.5482°N, 88.356°E). The images are acquired under a tropical climate (Dasgupta *et al.* 2013) with CGEPro (14'') 1400 HD Celestron telescope, charge coupled device (CCD): SBIG STT-8300 and RGB filters. The geographical location of the observational site and the climate

introduce an enormous amount of noise to the images. All of the images are captured in 16 bits per pixel and are 3358×2536 in dimension. The interface between the CCD and the computer stores those images in 32 bits per pixel. As we embark on reduction and analysis of the data, the usual photometric tasks: dark frame subtraction and flat frame division are not always capable to ameliorate the quality of the noise-infested images.

In an image, the level of details varies from location to location. Hence, one single optimal resolution is not suitable to analyze and operate on the image. A multiresolution representation of an image provides a complete idea about the extent of the details present at different locations in that image (Mallat 2008; Resnikoff *et al.* 2012). Therefore, the motivation behind this work is to incorporate a multiresolution framework in the processing method so that we can select and work on desired details as required. Wavelet transform is one of the many ways to achieve multiresolution representation of an image (Strang 1989, 1993). We employ multiresolution analysis based on wavelet transform to enhance the image quality. This facilitates further analysis to deduce stellar parameters, even from observations done under an extreme set of adverse conditions like ours.

This paper is organized as follows. In Section 2, we concisely discuss our observational work along with the details of the star cluster we observed. In Section 3, we briefly mention the noises present in the observed images. Section 4 discusses the need for alternate image processing techniques over the conventional dark frame subtraction, flat frame division. In Section 5, we discuss the role of multiresolution analysis along with the mathematical framework of the suitable processing method for our data. In Section 6, the role of the thresholding function and the modified thresholding function are explained. Section 7 presents raw images obtained from the ground-based optical observatory, then the processed images both in the conventional processing method and our proposed processing method. It also contains our discussion about the results of the improvement in the recognizability of stars. We also explore the possible improvement of the colour-magnitude diagram plotted using the data from our processed images. Finally, we summarize the paper in Section 8.

Throughout this paper, we are going to address the dark frame subtraction, followed by flat frame division as the ‘Standard’ processing method. Our proposed ‘High Noise Small Telescope Data’ processing methodology will be addressed as an ‘HNSTD’ processing scheme.

2. Observation and survey constituents

The observation was carried out in between the period of December 2017 to the 2nd week of March 2018. We observed for 25–30 nights. Among those nights, images of the NGC 2301 cluster were captured successfully on only 5 nights due to the drastically adverse seeing condition. The weather conditions in Kolkata did not permit us to observe prior to this. A couple of days before and after the full moon were not considered for stellar observations. Due to the air mass, atmospheric extinction plays a major role when one observes objects close to the horizon. The air mass evolves through the atmosphere because the light path is large closer to the horizon. A larger path involves proportionally more air mass and extinction will be higher. This forced us to choose targets which stay between not more than an angle 40° of zenith at that particular period. The list for observations was compiled from sources available in different pieces of literature (Grubissich & Purgathofer 1962). In Table 1, we present the details of the cluster analysed in this paper. For a distinct star cluster, three types of images were taken: raw images, dark images and flat images. Twenty–thirty sets of each image were taken for every type with blue, red and green filters separately. For a distant astronomical object, a long exposure time is needed. Instead of taking a single long exposure time image, we took an image of short exposure time and binned the suitable sets later during image processing. A 10 min exposure at a stretch of the NGC 2301 cluster results in excessive background levels from light pollution and dark noise. The details about noises are discussed in Section 3. We took the longest possible exposure for our case which was twenty separate 30-s exposure images as after that too much noise was appearing in the image. Combining these exposures got us close to the signal of a single 10-min image. We did not make copies of an image

Table 1. Details of NGC 2301 open star cluster acquired from available sources.

Parameter	Details
Constellation	Monoceros
RA	06 h 51 m 45 s
DEC	+00 27' 36"
Epoch	J2000
Members	96 ± 17
Distance	872 pc
Estimated age	165 millions years
Distance modulus [mag]	9.79

and then combine them to reduce noise. The images were taken separately and then combined to reduce noise. This was done since the noise in one image tends to cancel some of the noise in the other images. No cancellation can occur if the images are identical. Multiple images also allowed us to choose how to combine them based on the results we got. From these multiple numbers of images, we discarded the bad images and summed the best ones. All images were taken in flexible image transport system (FITS) format.

3. Noise details in images

The actual noise distribution in the astronomical CCD images is a complex sum of the Poisson photon noise plus different noises from various sources such as from the charge transfer, read-out electronics and others (Faraji & MacLean 2006). In our study, the position of the observational site and climate have introduced immense noise into the images. Among those various noises, the most notable ones are dark noise and flat field noise. The appearance of the dark frame depends on the characteristics of the CCD chip. It also depends on the temperature of the CCD chip at the time the dark frame is taken along with the exposure length. Dark noise generates out of the thermal noise of the CCD chip even in darkness. This will contribute to the overall estimated signal. The total number of electrons originated in a second depends on the operating temperature of the CCD. At the time of our observation, the background temperature was $\sim 10^\circ\text{--}16^\circ\text{C}$. The dark frames were taken as close as possible in time of light frames as chip characteristics do not change quickly, but they do change over time. To take a dark frame the shutter of the camera was closed and an image with the same exposure time as the light frame was taken, given in Figure 1. In Figure 2, we show the distribution of hot pixels' values (ADU) from a single dark frame image. The histogram gives a reasonable fit following the work reported in various literature (Pan *et al.* 2016; Atkinson *et al.* 2017).

If dark frames are the way to improve electronic noise then flat fields (Figure 3) are the process for cleaning up certain kinds of optical difficulties. To take a flat field image, we took an image of an evenly illuminated object that is an evenly illuminated sky just before dusk. Flat fields were taken at shorter exposures than light frames. For us at the time of taking a flat frame, the shutter speed was 1 s. Figure 4

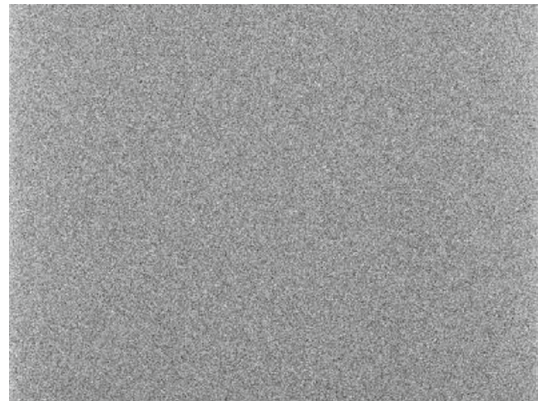


Figure 1. Single dark frame image recorded at background temperature $14^\circ\text{--}16^\circ\text{C}$, exposure time 30 s.

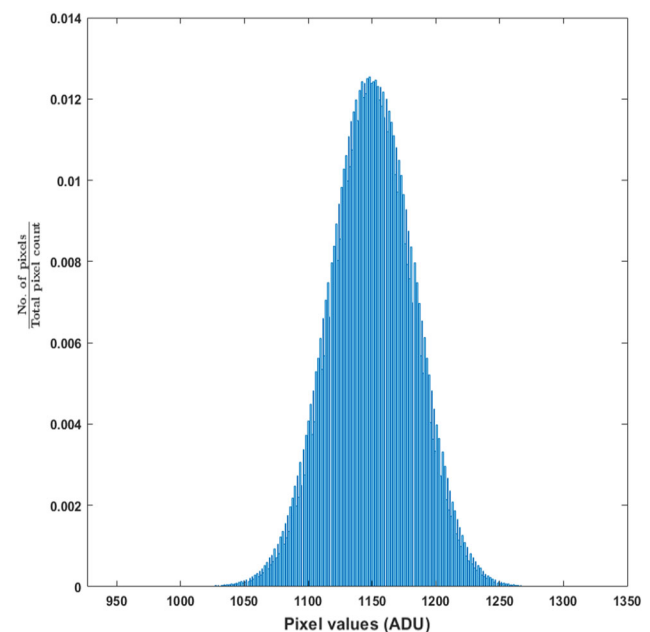


Figure 2. Histogram of single dark frame image as shown in Figure 1.

depicts the distribution of hot pixels' values (ADU) from a single flat frame image. The histogram exhibits a Gaussian kind of nature approximately. Vignetting, effects of Dust and no internal reflections were noticeable at the time of photographing the flat field's optical footprint.

4. Necessity of new image processing technique

There are a plethora of noise sources that deteriorates the quality of the images obtained by a CCD. A portion of these noises can be controlled up to a certain extent by taking some preventive measures during the time of the image acquisition, but some noise still



Figure 3. Flat field image of an evenly illuminated dusk sky recorded at exposure time 1 s. It shows some vignetting and quite a few dust motes, but no sign of any significant internal reflections.

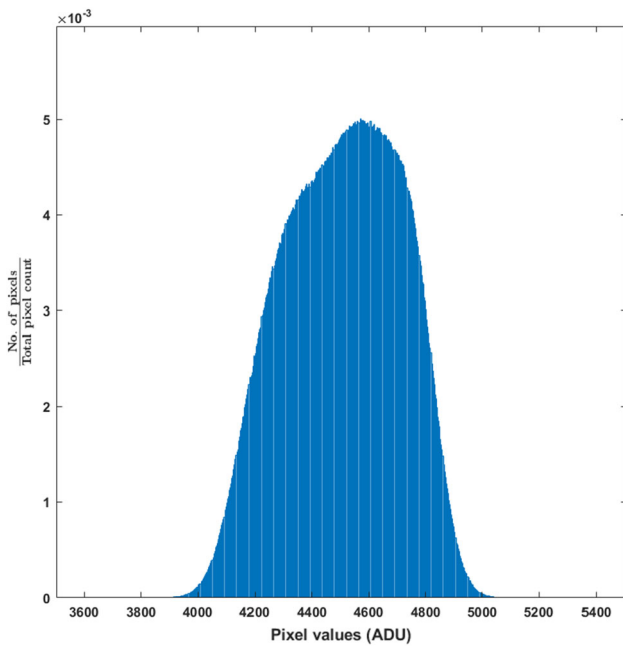


Figure 4. Histogram of single flat frame image as shown in Figure 3.

manages to damage the required features of the image. The denoising process enhances the image quality in some predefined sense. The ‘predefined’ quality is to be highlighted here because we are the ones who decide what the criterion of a good image should be (Gonzalez & Woods 2008). In the case of astronomical images, the foremost criterion is to retrieve proper flux of stars which was masked behind the noise. The most common technique to deal with the noises in astronomical images is dark frame subtraction followed by flat frame division, i.e., the standard processing technique. Though this process is quite

effective but under our observational circumstances, this technique fell short to yield the desired results.

In Figure 5, an example of the noise present in the raw image and the effect of the standard processing method are shown (details about the images with the respective position can be seen in Section 7). Table 2 describes the distinct positions marked in Figure 5 as an example. From Figure 5, we can observe that there are some pesky white granules in the raw images. After the standard image processing, they sustain their presence in the resulting image too but in a lesser quantity. Further, calculating the value of the noise granules with a fixed aperture 20 on the same position for both raw and standard processed image, we find that the pixel values of noises reduce by a significant amount for every filter (Table 2). However, along with the intensity of the noise, the standard technique also decreases the intensity over the entire frame. Thus, some faint objects become undetectable in the standard processed image. Such ramifications of standard processing are further elaborated in Section 7 with the help of results. This spatial domain approach of denoising lacks accuracy essentially in the noise processing itself. This process can be marked as an extensive averaging process where a frame of randomly generated hot pixels, i.e., a dark frame, is subtracted from the image followed by a flat frame division. This is very effective when noise is low but not for our image, where noise takes up a significant pixel value. Furthermore, this approach does not consider the different features present in the images explicitly. An image has some portions where intensity varies slowly (e.g., clear sky in an image) and some portions where intensity values change abruptly (e.g., the borders which distinguish the separation of the stars and the sky). As the frequency is directly related to spatial rates of change, intensity variation in the spatial domain can be associated with the frequencies in the Fourier transform of the image (Gonzalez & Woods 2008). If $i(x, y)$ be an image, and its Fourier transform be $I(u, v)$, then the slowest varying frequency component ($u = 0, v = 0$) is proportional to the average intensity of the image. Going away from the origin of the transform, the low frequencies are associated with the slowly varying intensity portions of the image and the high frequencies are associated with the rapidly varying intensities. In most cases, the majority of the noise is present in the region of high frequencies in the image’s spectrum. Therefore, directly subtracting the dark frame from an image is unable to tackle those specific higher frequencies, as no information about frequency is

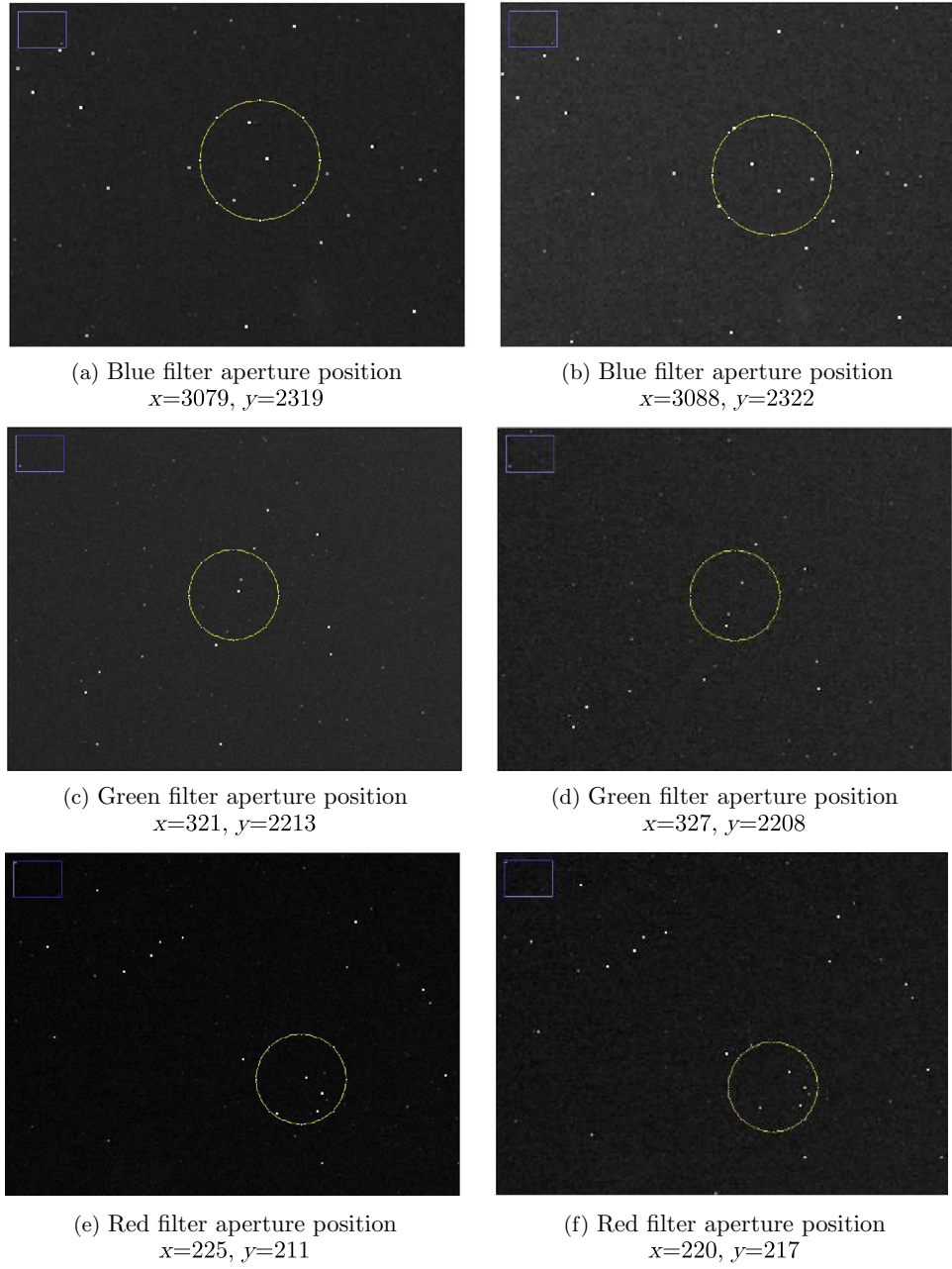


Figure 5. Example showing the effect of the standard image processing method on noise for three different filters at the mentioned position with fixed aperture 20. The left side represents noise data for the raw image. The right side represents noise data for processed (standard method) image. Quantitative description of the marked portion is shown in Table 2.

readily available in the spatial domain. The immediate alternate action of choice seems to be taking the Fourier transform of the image and performing various filtering in the frequency domain to diminish specific frequencies and then getting back the original image by inverse Fourier transform. However, in doing so, all the spatial information is lost when we move into the frequency (spatial frequency for images) domain. It can not be determined exactly where in the image some specific frequencies occur. This

problem of localization in both domains is present in many different aspects of nature: uncertainty between position and momentum, the uncertainty between time and frequency, the uncertainty between spatial domain location parameters and spatial frequencies in images. In all these cases, whenever we try to pinpoint a specific point in one domain, we need to span all over the other domain. This is best illustrated with the example of a Fourier transform of delta function. Delta function in any domain is localized at only one

Table 2. Effects of standard processing technique in noise suppression. The demerit is: the technique decreases the intensity throughout the image making faint objects undetectable (see Figure 16 for more details).

Image	Position		Noise intensity
	x	y	
Blue filter raw image	3079	2319	55354
Blue filter processed image	3088	2322	0
Green filter raw image	321	2213	52295
Green filter processed image	327	2208	2
Red filter raw image	225	211	63424
Red filter processed image	220	217	2

point, whereas its Fourier transform shows a corresponding signal to be spread over on the other domain.

5. Multiresolution image processing

The areas of an image containing significant details require high resolution for analysis and for the other areas a coarse representation is sufficient. Multiresolution analysis (Mallat 1989; Cohen 1995) facilitates us with a framework to analyze an image at different resolutions. Background literature (Daubechies 1992; Strang 1993; Vetterli & Kovacevic 1995; Mallat 2008; Resnikoff *et al.* 2012) suggests that analysis using a wavelet basis is a fine tool to obtain representations of an image at different resolution levels. In wavelet transforms, a wave of small duration, i.e., a wavelet, is used as a basis. As the wavelet can be scaled and shifted around (Strang 1989), the transform unveils various localized features to us. Among various kinds of wavelet transform algorithms, the orthogonal discrete wavelet transform (DWT) (Mallat 1989) and its biorthogonal variant (Cohen *et al.* 1992) are the most widely used. But they do not perform up to expectation in the case of astronomical images.

As we delve into the analysis with wavelets, we would like to clarify the meaning of three terms corresponding to the transform: scale, frequency, and resolution to avoid confusion. Scale in the wavelet transform of an image is well interpreted as similar to the scale in geographical maps. When a map is observed in high scales, only an approximate view of the region is seen (Tangirala 2018). Thus, there is a lower variation in data points, which implies lower frequency. The converse is true for the lower scales. So as the scale rises, we get lower and lower resolutions (Polikar *et al.* 1996; Tangirala 2018). The frequency corresponding to the wavelet transform represents the

spatial rate of changes in the image. For interpretation purposes, the scale and frequency can be perceived to be inversely related (Torrence & Compo 1998; Tangirala 2018). The term ‘resolution’ is particularly helpful while discussing images. The higher the resolution of the image, the finer the details we can extract from the image. In this paper, we would mostly discuss in terms of resolution, but in some cases, we would use ‘scale’ to explain mathematical expressions.

Several deficiencies of DWT on astronomical images have been found (Starck *et al.* 1995): in 2D DWT the wavelets are anisotropic. At each scale, horizontal, vertical and diagonal wavelets generate three wavelet coefficient sub-images, respectively. As the astronomical images have mostly isotropic objects, an isotropic wavelet is more suitable. Furthermore, traditional DWT is sensitive to the translation or shift of the input signal. The energy distribution of two wavelet coefficients differs significantly even if the input signal is shifted slightly by time or space. This drawback can bring serious problems while using the DWT on astronomical images. Along with this DWT suffers from other notable problems such as scale separation, presence of point objects and negative values at the output signal.

To resolve this issue with the application of DWT, new wavelet transforms have been developed based on continuous wavelet transform (CWT) by accepting a considerable amount of redundancy in the transformation. CWT needs to be discretized in order to implement it on a computer. The à trous algorithm (Holschneider *et al.* 1990; Shensa 1992) provides a discrete approach to such redundant wavelet transform. In this algorithm, the decimation is eliminated and this transform has the translation invariance property. Using a B-spline of order 3 in the à trous algorithm, Starck *et al.* (2010) introduced an isotropic undecimated wavelet transform which suited the requirements to be applicable on astronomical images.

Thus, this wavelet transform was also named as Starlet transform.

In this transform, a one-dimensional cubic spline function has been used as a scaling function (Figure 6).

$$\phi(x) = \frac{1}{12} (|x-2|^3 - 4|x-1|^3 + 6|x|^3 - 4|x+1|^3 + |x+2|^3), \quad (1)$$

$$\phi(x, y) = \phi(x)\phi(y). \quad (2)$$

The wavelet function is defined as the difference between two resolution levels

$$\frac{1}{4}\psi\left(\frac{x}{2}, \frac{y}{2}\right) = \phi(x, y) - \frac{1}{4}\phi\left(\frac{x}{2}, \frac{y}{2}\right). \quad (3)$$

The related analysis filter bank is defined as following:

$$h_{1D}[n] = \left[\frac{1}{16}, \frac{4}{16}, \frac{6}{16}, \frac{4}{16}, \frac{1}{16} \right]. \quad (4)$$

For two dimensional cases, the filter is designed to have separability property for faster and easier computation:

$$h_{2D}[k, l] = h_{1D}[k]h_{1D}[l], \quad (5)$$

$$g[k, l] = \delta[k, l] - h_{2D}[k, l], \quad (6)$$

where $\delta[k, l]$ is 2D unit impulse.

In case of an image, a 2D FIR filter response, h_{2D} can be generated as:

$$\begin{aligned} & \frac{1}{16} \begin{pmatrix} 1 \\ 4 \\ 6 \\ 4 \\ 1 \end{pmatrix} (1 \ 4 \ 6 \ 4 \ 1)/16 \\ &= \frac{1}{256} \begin{pmatrix} 1 & 4 & 6 & 4 & 1 \\ 4 & 16 & 24 & 16 & 4 \\ 6 & 24 & 36 & 24 & 6 \\ 4 & 16 & 24 & 16 & 4 \\ 1 & 4 & 6 & 4 & 1 \end{pmatrix}. \end{aligned} \quad (7)$$

Based on this framework, we used the Starlet transform algorithm (Starck *et al.* 2010) on a raw image to obtain transform coefficients: $W = \{w_1, w_2, \dots, w_J, c_J\}$. Here, w_1, w_2, \dots, w_J are the detail coefficients or wavelet coefficients and c_J is the coarse version of the original image (Figure 7). All the coefficients are of the same dimension as the original image.

The image can be easily reconstructed by the simple addition of the detail coefficients and the final

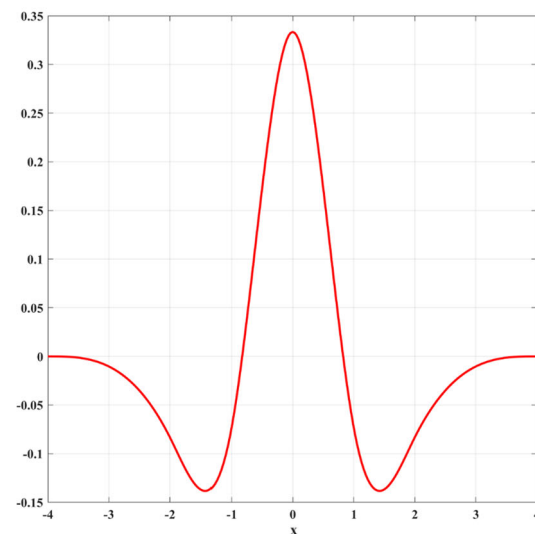
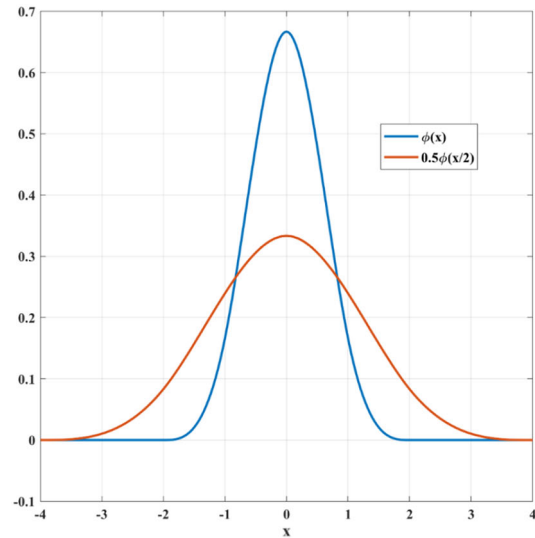


Figure 6. (i) One-dimensional cubic spline (scaling function) at two different resolution levels $\phi_{1D}(x)$, $\phi_{1D}(x/2)$ and (ii) a one-dimensional wavelet function $\psi_{1D}(x/2)$.

coarse sub-band:

$$c_0[x, y] = c_J[x, y] + \sum_{i=1}^J w_i[x, y]. \quad (8)$$

In Figure 7, it has been shown how the detail coefficients $\{w_i\}$ are capturing the fine details that exist between two resolution levels. The w_1 contains the finest of the details present in the image, while w_2 and w_3 contain comparatively less finer details, respectively, as can be seen in Figure 8(a–c). The c_3 is an approximate version of the image, i.e., the image at a lower resolution. For our images, if we continue to lower resolutions, e.g., c_4 , c_5 and compute $w_4 = c_3 - c_4$, $w_5 = c_4 - c_5$, there would hardly be any new information about the fine details left to be captured (because fine details are captured in higher resolutions,

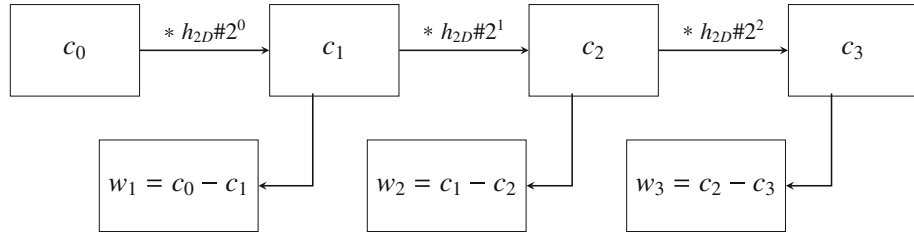


Figure 7. Multi-resolution decomposition by Starlet transform. The $\#2^i$ denotes the number of gaps between samples of h_{2D} and the $*$ denotes convolution operation.

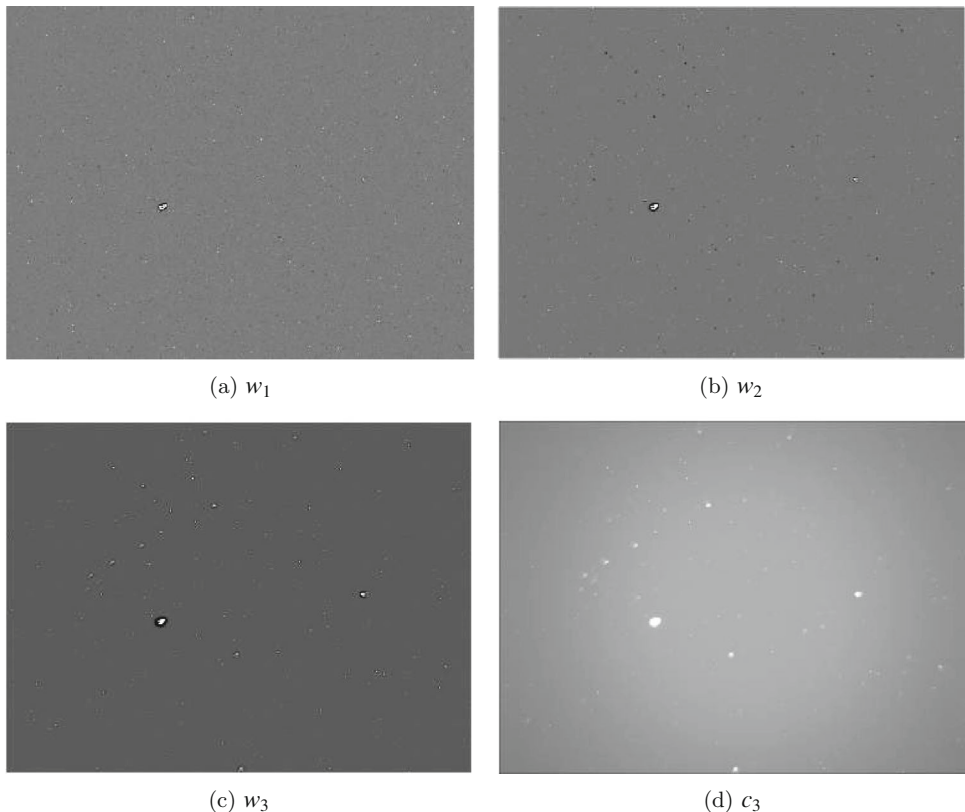


Figure 8. Result of multiresolution decomposition of observed star cluster NGC 2301 image over red band. Three detail coefficients ordered by decreasing spatial frequencies are shown along with the coarse approximation.

i.e., lower scales). If we observe Figure 8(d), we can see that c_3 , i.e., the coarse version of the image is already quite clear of noise and fine details. Hence, for our images, we decomposed each raw image into three detail coefficients (Figure 8a–c) and one coarse approximation coefficient (Figure 8d).

6. Image enhancement

To enhance the image, it needs to be manipulated by a function or functions so that the processed image is more suitable for our specific application, i.e., to plot the colour-magnitude diagram as accurately as possible. Once

the image is decomposed into transform coefficients corresponding to different resolutions, a suitable thresholding function can be used to modulate those coefficients to subdue the effects of noise.

In our images, the notable noises polluting the data (dark noise, optical noise, etc.) are Gaussian in nature, as mentioned in the noise details section before. The histograms of the single raw image in RGB filters separately are found to be approximately Gaussian in nature (Figure 9). After stacking multiple images, the nature of the histogram deviated slightly from the ideal Gaussian characteristics but can be approximated to be an ideal one. In Figure 10, histograms of the detail coefficients are shown separately.

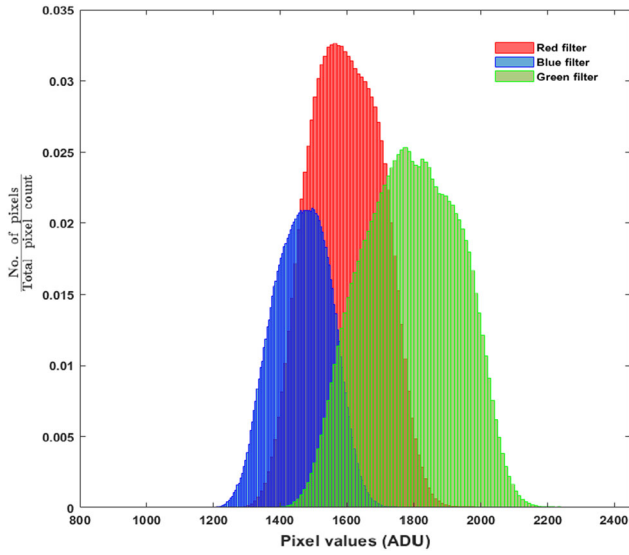


Figure 9. Histograms of single raw images of star cluster NGC 2301 over red, green and blue bands separately.

Under the condition of stationary Gaussian noise, the optimum comparison constant for the thresholding function can be selected as $3\sigma_i$, where σ_i is the noise standard deviation at each resolution level i . The value $3\sigma_i$ is chosen from the empirical rule which dictates that for a Gaussian distribution, nearly 99.7% values lie within three standard deviations of the mean (Gonzalez & Woods 2008). In Section 5, we discussed how the wavelet transform captures the fine details of the image within the detail coefficients $\{w_i\}$. The approximation coefficient only gives an overall idea of the image's content without any details. As most of the fine details in our images are induced by the different noises, those components are sifted out in the detail coefficients corresponding to higher resolutions. Thus, it is adequate to compare each element of the detail coefficient matrices (w_1 , w_2 , w_3) with $3\sigma_i$.

Now, the orthodox hard thresholding method introduced by Donoho & Johnstone (1995), is as follows:

$$\begin{aligned} w'_i(k, l) &= w_i(k, l), & \text{when } |w_i(k, l)| \geq 3\sigma_i \\ &= 0, & \text{when } |w_i(k, l)| < 3\sigma_i. \end{aligned} \quad (9)$$

The characteristics curve of this thresholding function is shown in (Figure 11). However, in case of our images, this hard thresholding procedure is found to be inadequate to enhance the image quality for further work (Figure 12).

The reason behind this predicament lies within the nature of our image. If we observe the raw image (Figures 5a,c,e and 15), we can see that most of the noise manifested in the image as very fine and sharp,

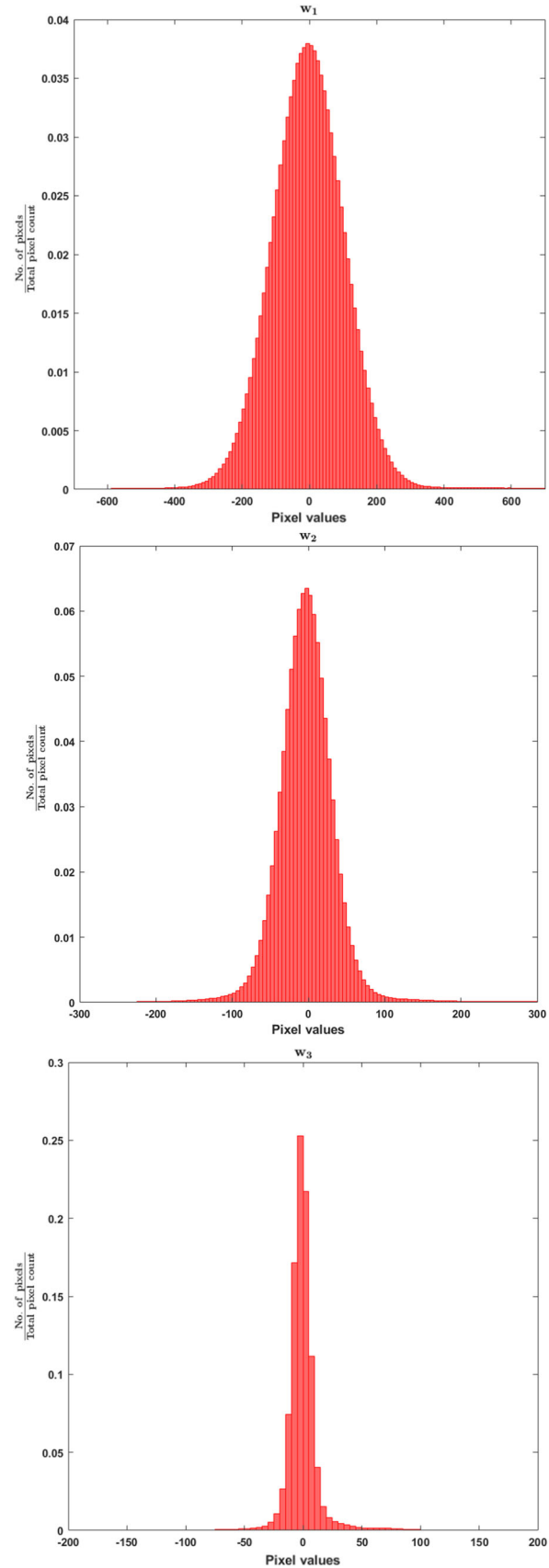


Figure 10. Histogram of each detail coefficient w_1 , w_2 , w_3 , respectively, of raw NGC 2301 image over red band.

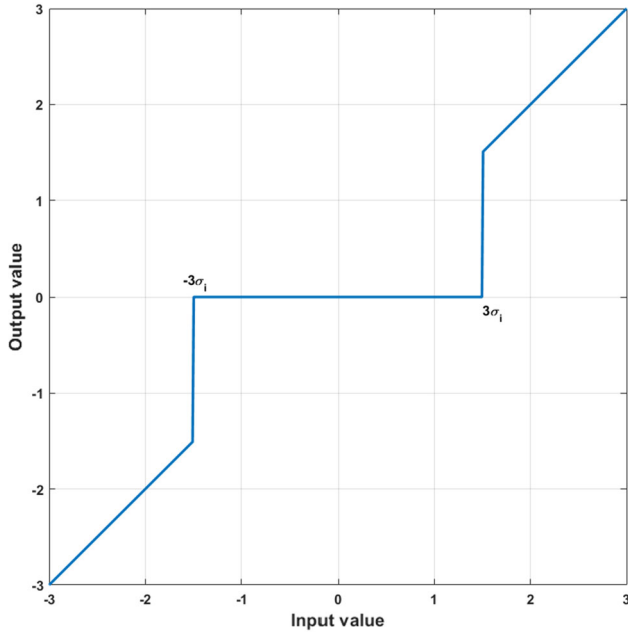


Figure 11. Orthodox hard thresholding characteristics (cut-off points $|3\sigma_i|$ are marked).



Figure 12. Example of an NGC 2301 star cluster image (red band) processed using orthodox hard thresholding method (not satisfying required quality). To inspect the image details one should zoom in to a significant extent.

white granular quantities. Those white granular quantities appear in smaller sizes than the actual stars, but they are brighter and more intense. The smaller size and sharp, intense nature of these white grains are making them a part of the detailed features present in the image. Whereas, the fainter stars are acting like background objects. Also, as discussed in the earlier Section 4, these white grains are causing abrupt changes in the image. That's why when we break the raw image into different resolution levels, these granular noise quantities are dominant in the detail coefficients, especially in w_1 (Figure 8a), w_2

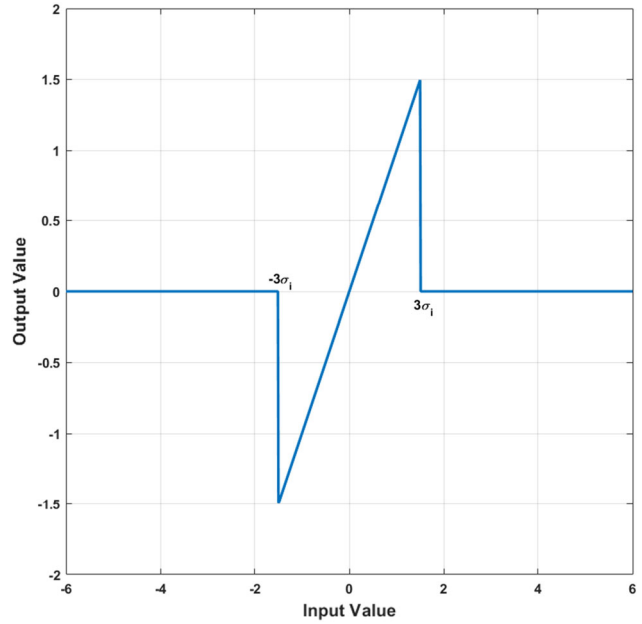


Figure 13. Modified hard thresholding characteristics (cut-off points $|3\sigma_i|$ are marked).

(Figure 8b) and we can see that in the coarse representation of the image, c_3 (Figure 8d) the stars are dominant. Therefore, the motivation behind our modification to the hard thresholding function (Equation 9) is: in the detail coefficients, the noise will give rise to very high, dominating values. Retaining most of the information about the stars intact within the boundary of $3\sigma_i$, we can detach those high values from each detail coefficients.

The modified thresholding function is given as:

$$w'_i(k, l) = 0, \quad \text{when } |w_i(k, l)| \geq 3\sigma_i, \\ = w_i(k, l), \quad \text{when } |w_i(k, l)| < 3\sigma_i. \quad (10)$$

Figure 13 depicts the characteristics curve of this modified thresholding function.

The values of σ_i are obtained from the standard deviation of the noise σ_s in the original image. In an ideal case where a noise-free image is available to us, a simulation can be performed by: 1) adding Gaussian noise of standard deviation 1 in that ideal image; 2) then splitting that noisy image using Starlet transform and from those, the standard deviation of each detail coefficient σ_i^e can be found. From the properties of wavelet $\sigma_i = \sigma_s \cdot \sigma_i^e$ (Starck & Murtagh 1994).

In our case, as we have obtained the cluster image from an on-site observation, an ideal image of the same characteristics is not available to us. This leads us to use a variance stabilizing transformation to modify our raw image data towards a data set such that its characteristic is a Gaussian distribution with standard

deviation as close as possible to unity. To achieve this we have used Anscombe transform (Donoho 1992):

$$Y_{i_1,i_2} = 2\sqrt{N_{i_1,i_2} + \frac{3}{8}}, \quad i_1, i_2 = 0, \dots, m-1, \quad (11)$$

where Y is the new data set and N is the old data set.

After applying the Anscombe transform on the raw image, we obtain the detail coefficients from the transformed image and estimate σ_i^e (Table 3).

The noise standard deviation σ_s is estimated from the finest resolution available in the detail coefficients using median absolute deviation σ_m (Donoho 1992).

$$\sigma_m = \frac{\text{MEDIAN}(|w_1|)}{0.6745}, \quad (12)$$

$$\sigma_s = \frac{\sigma_m}{\sigma_1^e}. \quad (13)$$

Now from this σ_s value, all the three σ_i values are calculated. Finally, after thresholding, the three new

Table 3. Table of σ_i^e , standard deviation of each detail coefficient of red, green and blue band images.

	Red	Green	Blue
σ_1^e	4.0895	4.1445	4.0559
σ_2^e	2.6428	2.7116	2.5197
σ_3^e	3.0281	3.0974	2.8435

detail coefficients and the coarse representation of the image are added together to get the final enhanced image.

Starting from the multiresolution decomposition in Section 5 to the modification with appropriate thresholding function, the overall proposed methodology is depicted in a concise block diagram given in Figure 14.

7. Results and discussions

The presence of enormous noise in the raw observed cluster images (Figure 15) has directed us towards a path to suppressing the noise yet getting the desired quality result. Figure 16(a,c,e) are the images processed by the standard method of dark frame subtraction and flat frame division. In Section 4 the underlying pitfall of the standard method is pointed out using specific portions of these images as an example. Figure 16(b,d,f) are the images processed by the proposed ‘high noise small telescope data’ (HNSTD) processing methodology. To evaluate the performance of the proposed method, we proceed to a meticulous comparison between the results produced by the two methods. As we are dealing with real-time onsite data, we don’t have an ideal image matching

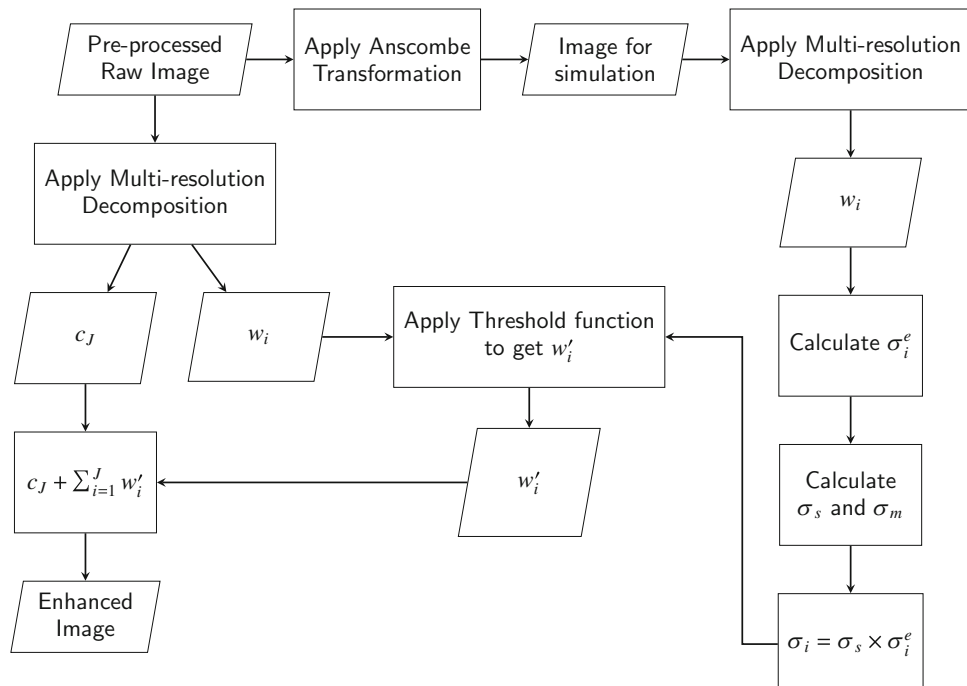


Figure 14. A diagram depicting the overall working of the proposed ‘high noise small telescope data’ (HNSTD) processing methodology.

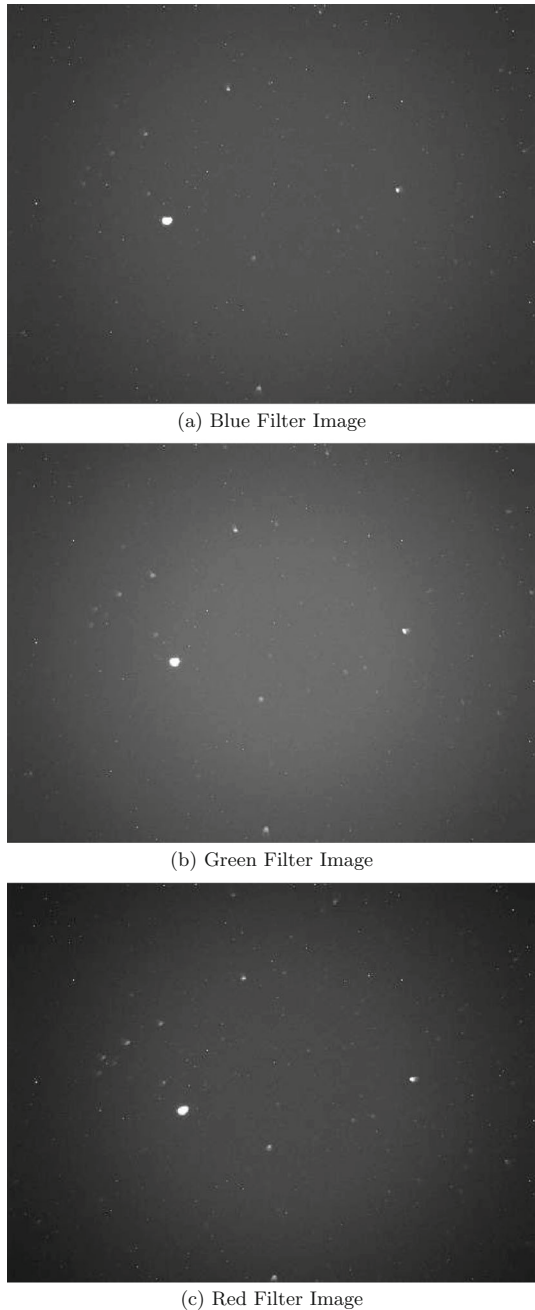


Figure 15. Example of a nearly 10 min exposure of NGC 2301 raw star cluster image, which was taken with an SBIG STT 8300 CCD camera through CCGEPro (14'') 1400 HD Celestron telescope at Fr. Eugene Lafont Observatory, St. Xavier's College, Kolkata ($22^{\circ}32'55.8''$ N, $88^{\circ}21'20.8''$ E). Upper left corner represent $x = 0$, $y = 0$ and lower right corner represent $x = 3358$, $y = 2536$.

the exact dimension of the acquired raw image. Hence, we take a subjective approach to evaluate the effectiveness of the HNSTD methodology.

The first subjective quality we rely upon is the visual perceptibility in the images. The images from standard

processing appear to have good contrast, but when zoomed into the Figure 16(a,c,e), we can see a notable amount of white granular noises are still present and several stars are not recognizable by either the human eye or software. If we zoom in the images produced by the HNSTD scheme (Figure 16b,d,f), we can see that most of those minuscule bright white grains have disappeared and a significant number of faint stars that were unrecognizable in Figure 16(a,c,e), are now recognizable in these images.

Table 4 presents a comprehensive, quantitative description of the recognizability of stars in red, green, blue filters using a standard star detection software Daophot II (Stetson 1987). Using Daophot II, we have documented the star detection process for RGB filters in the raw frame, standard processed frame, and HNSTD processed frame. All the parameters that are taken at the time of detection are given in this table. In Section 3, we outline working with severely noise-polluted images. Due to functioning exclusively in the spatial domain, the standard processing method decreases the intensity throughout those severely noise-infested images. As discussed in Section 4, what Table 2 shows for the noise granules also happens to all other objects in the frame. Inevitably the star intensities become so low that they descend below the detection threshold of Daophot II. That is reflected in the operation of Daophot II, where the stars' intensity diminishes so much that Daophot II can not even detect any star in the standard processed images. So to showcase the effectiveness of the HNSTD method, we have compared the number of stars detected by Daophot II in the raw images and the HNSTD processed images in Table 4. Histogram of star count with their V_J -magnitudes for raw and HNSTD processed images are given in the Appendix to compare the star count. As Daophot II is unable to extract any star data from the standard processed images, we have also carried out a manual detection to plot the colour-magnitude diagram for those images.

As a significantly large number of stars become recognizable in Figure 16(b,d,f), more data points are available to plot the colour-magnitude diagram. Figures 17 and 18 illustrate colour-magnitude diagrams of the NGC 2301 open star cluster, plotted using the data from images processed by the standard method and by the HNSTD scheme, respectively. The colour-magnitude diagrams are plotted with both the linear and isochrones fitting. B_J , V_J and R_C are the Johnson B, V and Cousins R magnitudes (Park *et al.* 2016). Here we attempt to find out whether further analysis is possible using the data from the HNSTD processed

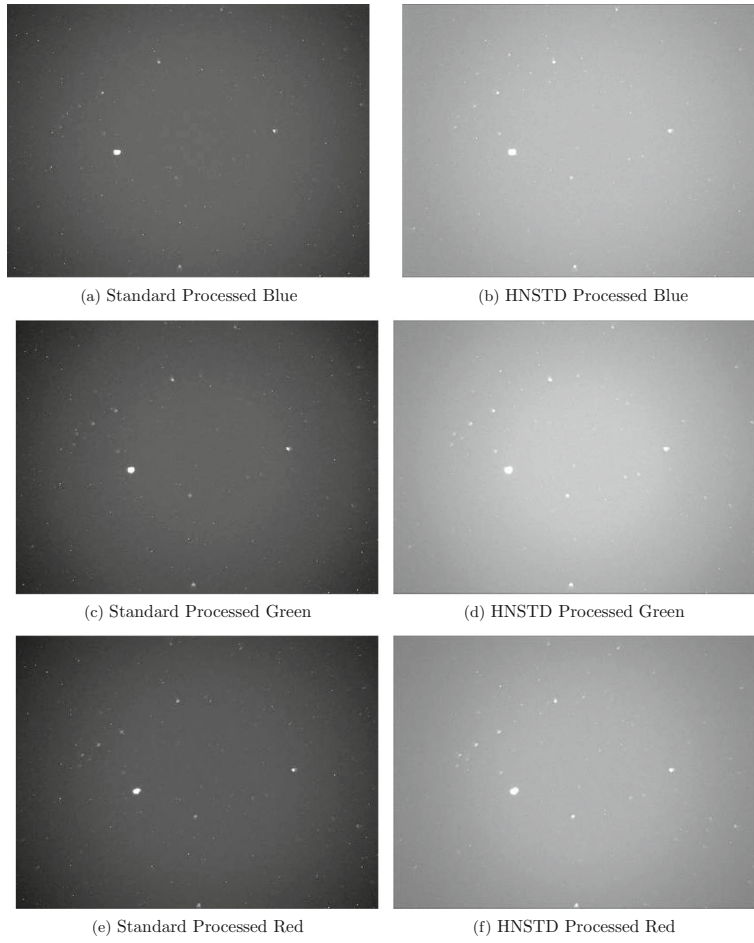


Figure 16. In the left side a, c, e are images processed by the standard method. In the right side b, d, f are the image produced by our HNSTD method. a, b are of blue filter; c, d are of green filter; e, f are of red filter. To inspect the image details one should zoom in to a significant extent. Upper left corner represent $x = 0$, $y = 0$ and lower right corner represent $x = 3358$, $y = 2536$.

Table 4. Comparing the recognizability of stars between raw, standard and HNSTD processing method using a standard star detecting software for different filters.

Details of star detection software	Filter	No. of stars detected in raw frame	No. of stars detected in standard frame	No. of stars detected in HNSTD frame
Daophot II (Stetson 1987)	Red	397	No detection	903
Readout noise = 27.027				
Gain (e/ADU) = 0.37	Green	663	No detection	945
Low good datum (σ) = 7.00				
High good datum (ADU) = 56000.00				
FWHM of objects (pixel) = 20.00	Blue	362	No detection	896
Threshold (σ) = 5.00				
Fitting radius (pixel) = 20.00				
PSF radius (pixel) = 50.00				

images and to showcase the improvement in this analysis procedure over the analysis done using the standard processed images. Isochrone fitting exhibits

that all the stars are essentially lying in the main-sequence region, with no main-sequence turnoff or new branching. Thus, it further justifies the linear fit

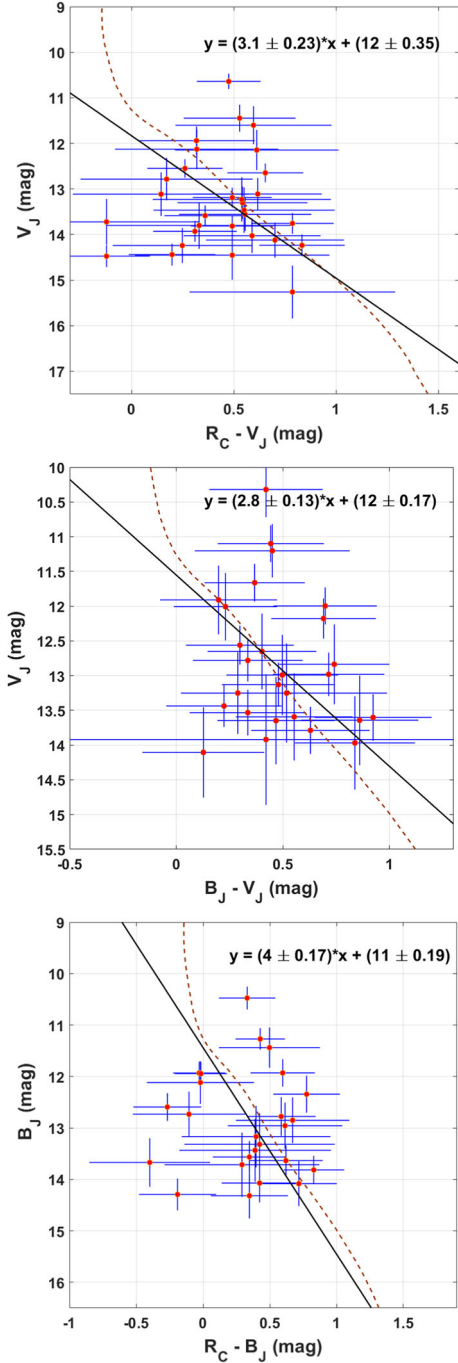


Figure 17. Three different colour magnitude diagrams of NGC 2301 open star cluster based on the standard processed image with both the linear and isochrones fitting. The number of detectable stars is less in this image as the standard noise processing method is inadequate for our highly noise polluted image and the colour magnitude diagrams are not very conclusive. The error bar indicates the propagating error associated with the measured flux.

model in the main-sequence region. We deemed it suitable to employ a linear fit which is normally mentioned in astrophysics textbooks for main

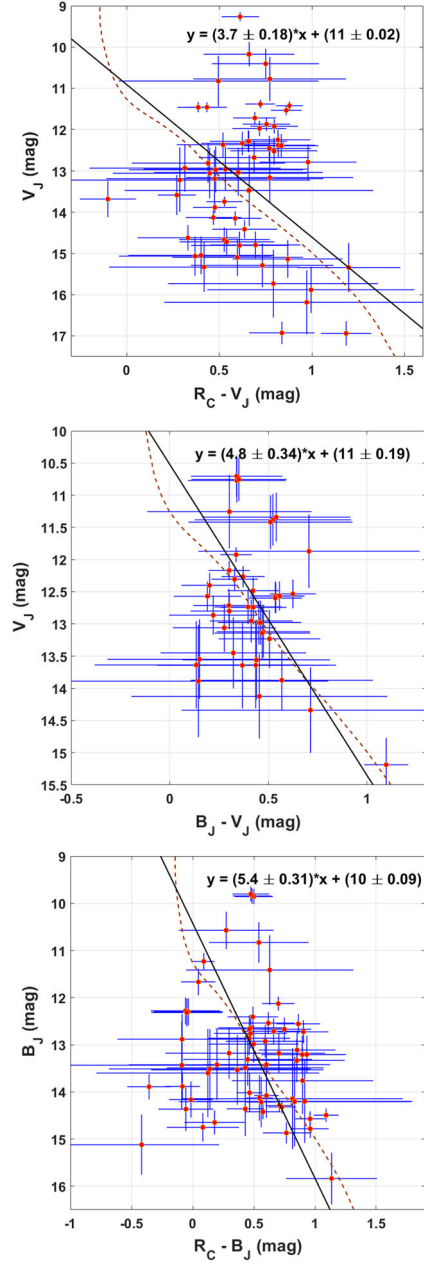


Figure 18. Three different colour magnitude diagrams of NGC 2301 open star cluster based on the image processed by the HNSTD processing with both the linear and isochrones fitting. The number of detectable stars has increased noticeably in this image which can be seen from the diagram and furthermore, the colour magnitude diagrams are comparable with the main sequence phase of an ideal colour magnitude diagram. The error bar indicates the propagating error associated with the measured flux.

sequence stars (Carroll & Ostlie 2006; Karttunen *et al.* 2016). We compare the improvement of the slope value (of the linear fits) between the standard and HNSTD methods (Table 5). It serves as a quantitative metric to demonstrate the improvement due to our

Table 5. Comparison between the slope values of the straight line fitted in the curve using the data from the standard processing method and the HNSTD processing method.

Colour magnitude diagram (mag)	Ideal value	Standard method	HNSTD method
$R_C - V_J$ vs V_J	6.04	3.1 ± 0.23	3.7 ± 0.18
$B_J - V_J$ vs V_J	6.04	2.8 ± 0.13	4.8 ± 0.34
$R_C - B_J$ vs B_J	6.04	4 ± 0.17	5.4 ± 0.31

methodology. For the main sequence curve, the slope of the straight line should be of value 6.04 (Karttunen *et al.* 2016).

More stars lie on the main sequence branch for Figure 18. The colour-magnitude diagram plotted using data from our HNSTD processing scheme is better to comment about the phase of the star cluster. The error bars in the colour-magnitude diagrams indicate the propagating error associated with the measured flux of a specific star during multiple measurements (Koppelman 2005).

8. Conclusion

In this paper, we have presented a denoising scheme for raw star cluster images taken from a site with many limitations. Over four months, the observational work has been done for the first time from Fr. Eugene Lafont Observatory St. Xavier's College (Autonomous), Kolkata. During observations, precise measures were taken to reduce noise as discussed in Section 2. The orthodox method of dark frame subtraction followed by flat frame division was not effective against the residual noise that persisted even after taking all the precautions. Being smaller in size than the stars, yet having more intense and sharper brighter character, those noise granules manifested as part of the detailed features present in the images. The much fainter and unrecognizable stars acted as background objects. Hence, a multiresolution approach was needed to split the images into different resolutions. Moreover, a modified thresholding function was designed to sift out the specific type of noise present in the images.

Our results champion the efficacy of the HNSTD methodology in several ways. The significant improvement in the recognizability of stars are further corroborated by the comparison between the color-magnitude diagrams plotted using data from images

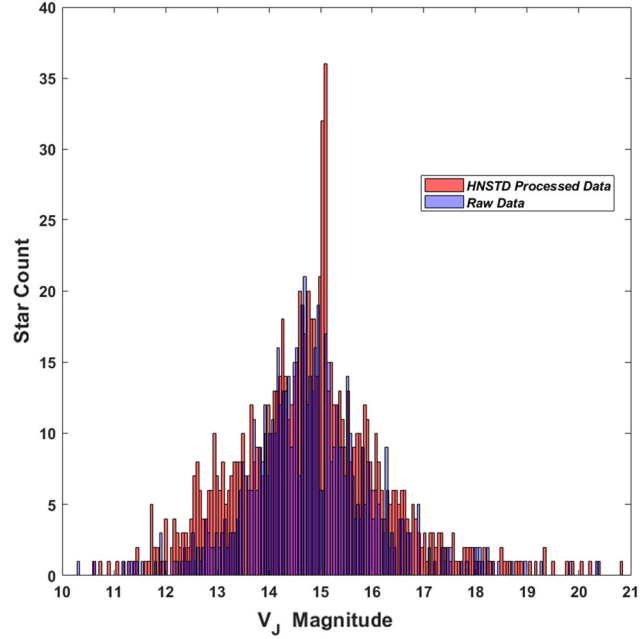


Figure 19. Two histograms depicting star counts for the HNSTD processed data and raw data as detected using Daophot II. V_J is Johnson V magnitude. The violet region represents overlap of data.

processed by the standard method (Figure 17) and the HNSTD method (Figure 18). Therefore, although observations were performed under not-so-ideal conditions, our proposed scheme produced significant improvement in the image quality subjectively.

In the future, the proposed HNSTD scheme can be used along with absolute photometry analysis to explore further parameters of any star cluster. Other multiresolution analysis methods can also be employed depending upon the features in the image, new custom-made wavelet basis can be explored as well. We hope that our work will motivate others to initiate small telescope observations from sites constrained by its geographical location.

Acknowledgements

The authors would like to thank Anjasha Gangopadhyay, faculty at Hiroshima Astrophysical Science Center, Hiroshima University, Japan, for valuable discussions and technical assistance for detecting stars using Daophot II. Special thanks to Subhash Bose, faculty at Department of Astronomy, The Ohio State University for insightful discussions on Johnson–Cousins BV R Filter System and isochrone fitting.

Appendix A. Histogram plots showing gain in star count

See Figure 19.

References

- Atkinson D. E., Hall D. N., Jacobson S. M., Baker I. M. 2017, *Astron. J.* 154, 265
- Carroll B. W., Ostlie D. A. 2006, An introduction to modern astrophysics and cosmology/BW Carroll and DA Ostlie. 2nd edition, San Francisco: Pearson
- Cohen A., Daubechies I., Feauveau J.-C. 1992, *Commun. Pure Appl. Math.*, 45, 485
- Cohen L. 1995, Time-Frequency Analysis/Leon Cohen. Prentice Hall PTR Englewood Cliffs, New Jersey, p 299
- Dasgupta S., Gosain A. K., Rao S., Roy S., Sarraf M. 2013, *Clim. Change*, 116, 747
- Daubechies I. 1992, Ten lectures on wavelets (SIAM)
- Donoho D. L. 1992, in Presented on the International Conference on Wavelets and Applications, Tolouse, France
- Donoho D. L., Johnstone I. M. 1995, *J. Am. Stat. Assoc.*, 90, 1200
- Faraji H., MacLean W. J. 2006, *IEEE Trans. Image Process.*, 15, 2676
- Gonzalez R., Woods R. 2008, Digital Image Processing 3rd Edition, 461
- Grubissich C., Purgathofer A. 1962, *Zeitschrift fur Astrophysik*, 54, 41
- Holschneider M., Kronland-Martinet R., Morlet J., Tchamitchian P. 1990, in Wavelets. Springer, 286
- Karttunen H., Kröger P., Oja H., Poutanen M., Donner K. J. 2016, Fundamental Astronomy. Springer, Berlin
- Koppelman M. 2005, *Soc. Astron. Sci. Ann. Symp.*, 24, 107
- Mallat S. 2008, A Wavelet Tour of Signal Processing, Third Edition: The Sparse Way. Academic Press, Inc., New York
- Mallat S. G. 1989, *IEEE Trans. Pattern Anal. Mach. Intell.*, 11, 674
- Miles R. 1998, *J. Br. Astron. Assoc.*, 108, 65
- Pan C., Weng F., Beck T., et al. 2016, in 2016 IEEE International Geoscience and Remote Sensing Symposium (IGARSS), IEEE, 1966
- Park W., Pak S., Shim H., et al. 2016, *Adv. Space Res.*, 57, 509
- Polikar R., et al. 1996, The wavelet tutorial, <http://users.rowan.edu/~Polikar/WTutorial.html>
- Resnikoff H. L., Raymond Jr O., et al. 2012, Wavelet Analysis: The Scalable Structure of Information. Springer, Berlin
- Saha S. K. 2002, *Rev. Modern Phys.*, 74, 551
- Shensa M. J. 1992, *IEEE Trans. Signal Process.*, 40, 2464
- Starck J.-L., Murtagh F. 1994, *Astron. Astrophys.*, 288, 342
- Starck J. L., Murtagh F., Bijaoui A. 1995, in Astronomical Society of the Pacific Conference Series, Vol 77, Astronomical Data Analysis Software and Systems IV, eds Shaw R. A., Payne H. E., Hayes J. J. E., p 279
- Starck J.-L., Murtagh F., Fadili J. M. 2010, Sparse Image and Signal Processing: Wavelets, Curvelets, Morphological Diversity. Cambridge University Press, Cambridge
- Stetson P. B. 1987, *Publ. Astron. Soc. Pac.*, 99, 191
- Strang G. 1989, *SIAM Rev.*, 31, 614
- Strang G. 1993, *Bull. Am. Math. Soc.*, 28, 288
- Tangirala A. K. 2018, Principles of System Identification: Theory and Practice. CRC Press, Boca Raton
- Torrence C., Compo G. P. 1998, *Bull. Am. Meteorol. Soc.*, 79, 61
- Vesperini E. 2010, *Philos. Trans. R. Soc. A Math. Phys. Eng. Sci.*, 368, 829
- Vetterli M., Kovacevic J. 1995, Wavelets and Subband Coding. Prentice Hall, Hoboken